



An adaptive optics aided differential optical positioning for passive orbit determination of the space debris at the geostationary orbit



Piotr Piatrou^{*}, Francois Rigaut

Research School of Astronomy and Astrophysics, Mt Stromlo and Siding Spring Observatories, ANU College of Science, Cotter Road, Weston Creek, Canberra, ACT, 2611, Australia

ARTICLE INFO

Keywords:

Space debris
Satellite tracking
Space surveillance
Adaptive optics
Image processing

ABSTRACT

Proliferation of space debris presents an imminent threat to all space assets. The problem is especially severe for the geostationary band of orbits (GEO) because the GEO objects never leave their orbit and, at the same time, are difficult to observe and operate due to large distance from the Earth. Under the influence of tidal forces, even passive GEO objects achieve high local velocities without vacating GEO positions, which may potentially lead to devastating collisions. Our ability to predict collisions in GEO is limited by the scarcity of the accurate orbital data, especially about the small and passive objects. The efforts to address this omission strongly rely on the ground-based optical sensors and, consequently, on the efficient space object detection and tracking techniques. In this paper we propose a passive differential optical debris tracking technique combining adaptive optics and a high accuracy astrometric references resulting in a significant improvement in the GEO object positioning accuracy. The achievable accuracy is estimated via detailed numerical simulations of two telescopes in different locations.

1. Introduction

The ever-growing number of space debris is a global and imminent threat affecting nearly all the assets located in space. The problem is even more severe for the Geostationary band of orbits (GEO), arguably the most precious part of the Earth's neighborhood because of its unique properties and dense population. The rate of accumulation of space debris on GEO is higher because unlike the lower orbits which decay with time the GEO objects stay there forever. As it is pointed out in Ref. [1], despite the quite low collision probability estimate for GEO objects based on the current incomplete data about the GEO population is quite low, taking into consideration the (mostly unknown at present) small objects of the size in 10 cm - 1 m range may well increase the collision probability significantly. Our ability to predict collisions in GEO is limited by the accuracy of the orbital data available, especially for the debris which are smaller than the operational satellites and thus have low brightness. The deficiency of the space debris tracking information drives the need for additional ground-based measurement facilities such as the International Scientific Optical Network [2] or the prospective European Space Surveillance System [3].

Passive optical sensors appear to be the only reliable means for the purpose because of long distance to the GEO objects. Their performance

[4,5] is fundamentally limited by three factors: the photon flux reflected from the Sun-illuminated objects, atmospheric seeing and positioning errors of the telescope mount. The first limit can be pushed by the use of larger ground-based telescopes and by longer observations, the second one by the use of Adaptive Optics (AO) [6] and other turbulence compensation techniques such as Speckle Interferometry [7,8], the third one by switching from a telescope mount as an angular measurement reference to highly accurate astrometric references whose appearance is anticipated in the nearest future.

In this paper we propose a passive differential optical tracking technique for the GEO objects combining AO and an extremely accurate astrometric references provided by the GAIA mission [9]. We prove through the numerical simulations the capability to achieve 40 milli-arcsecond (mas) accuracy on GEO objects as deemed as 15th visible magnitude for the 1.8-meter EOS telescope at Mount Stromlo Observatory (MSO) in Australia (relatively high 35° latitude) with AO, and roughly the same accuracy at 19th magnitude for the 3.8-meter UKIRT telescope [10] at Mauna Kea Observatory (MKO) in Hawaii (19° latitude) without AO.

In what follows we are going to present the theory of optical differential debris positioning and the factors driving its feasibility (Section 2). Section 3 describes the prospective laser guide star (LGS) AO system to be

^{*} Corresponding author.

E-mail addresses: piotr.piatrou@anu.edu.au (P. Piatrou), francois.rigaut@anu.edu.au (F. Rigaut).

installed on the 1.8-meter telescope at MSO and expected to play a prominent role in the high-accuracy debris tracking. Section 4 describes in detail the positioning algorithms used in our analysis. Section 5 presents the results of the end-to-end simulations of the optical positioning system working in two significantly different but equally favorable sets of conditions: 1) a small telescope equipped with the efficient AO system operating in bad atmospheric turbulence conditions and 2) a large telescope without AO operating in exceptionally low turbulence. A value of the AO turbulence correction impact on the optical tracking accuracy is also estimated as a side product of our investigation.

2. The idea of differential debris positioning

In order to significantly improve positioning accuracy the proposed debris positioning method tries to exploit a combination of the following mutually connected ideas:

- to overcome the accuracy limit of the telescope mount positioning an external astrometric reference (a star) with celestial coordinates known to high accuracy can be observed together with the space object;
- if the space object and the reference star are observed simultaneously in the telescope field of view (FoV), position can be measured as a difference between the known reference star and the object; the differential nature of the measurement allows to eliminate the tip-and-tilt errors due to the telescope vibrations and the atmospheric turbulence (provided the exposure time is short enough);
- instead of a long continuous exposure necessary to observe a dim space object a long series of short exposures are used to take full advantage of the differential position measurement;
- to avoid excessive noise associated with multiple camera reads, extremely low-noise Electron-Multiplying [11,12] CCD or the CMOS cameras [13] that have recently become commercially available are used for simultaneous space object and reference star imaging; the image accumulation is performed in software using a special integration algorithm;
- finally, to eliminate the blurring effect of atmospheric turbulence, improve image sharpness and signal-to-noise ratio Adaptive Optics is used.

Note that the use of astrometric references instead of mechanical ones for accurate celestial object positioning as such is not a new idea and appears to be a routine method for image post-processing [14]. We however point out that it is the combination of the aforementioned techniques: large telescope with AO and short exposures (thus high potential image position accuracy) and the highly accurate star catalogs not available in the past that makes the achievable accuracy go far beyond the limits of the telescope mount positioning.

Obviously, applicability of each technique mentioned above has its limits. Here we can give a brief summary of the difficulties associated with the proposed approach, which will be addressed in more detail below:

- The availability of astrometric references is limited not only by their accuracy but also by the density of the stars with brightness high enough to be observable within the telescope opto-electronic system technical limitations. Density of the star field within the range of trajectories of the Geostationary space objects is a crucial parameter for the orbit determination and has to be carefully estimated.
- Atmospheric turbulence has triple effect on the positioning accuracy:
 - 1) turbulence-induced blurring reduces image sharpness thus reducing spot positioning accuracy, and due to distribution of the object image over larger number of pixels the readout noise is increased;
 - 2) turbulence-induced global image motion (tip and tilt, TT) can be “frozen” by short-exposure imaging, however, some residual

motion blur is always present reducing the positioning accuracy and signal-to-noise ratio (vibrations are alike but we leave them outside the scope of this paper);

- 3) turbulence-induced anisokinetism [15], i.e. decorrelation of the random tip-and-tilt motion between two points in the FoV, which makes it impossible to compensate tip-and-tilt for a pair of simultaneously observed objects (debris and reference star) even by the differential measurement, an error that cannot be compensated by means of AO.
- Capabilities of turbulence compensation by the AO system are also limited. In addition to inability to deal with anisokinetism, an AO system has limited resolution, signal-to-noise ratio, the anisoplanatic error limits the FoV within which AO compensation is efficient, which in turn limits the available observation time and data integration capabilities. In addition to it, availability of natural guide stars (NGS) that can serve as light beacons for the AO system wavefront sensors is severely limited. In no hope to achieve a reasonable sky coverage with NGSs, the AO system for space object observations has to resort to the artificial Laser Guide Stars (LGS), which have their own limitations: an additional focus anisoplanatism error due to finite LGS altitude, star elongation, fratricide and limited photon flux [16]. Generally speaking, sky coverage of the LGS-based AO is limited by availability of the NGSs needed for TT compensation because LGSs by their specific nature cannot provide tip-and-tilt information. Luckily enough, since the differential positioning is insensitive to TT, the LGS-based AO sky coverage can be considered unlimited in our case.
 - Positioning algorithm has a goal to integrate the information contained in each of multiple short-exposure frames into the final position estimate, detect outliers, perform de-noising and spot positioning with sub-pixel accuracy. Its efficiency has a direct impact on the final positioning error.
 - Clock and clocking errors are due to image timing inaccuracy (the former) and due to the fact that the image in the camera FoV rotates following the position of the telescope mount (the latter). The timing error can be estimated based on the fact that the fastest motion in the image is the reference star motion due to Earth rotation with velocity of $15''/s$ (whereas the GEO object is quasi-stationary) and, therefore, the typical clock error of $1 \mu s$ translates into 0.015 mas position error. The clocking error is more significant: image rotation (clocking) can be directly extracted as a side product of the reference star positioning process by watching the star motion in the sequence of images obtained during the reference and object simultaneous observation. Since the reference star is moving in the FoV due to Earth rotation, its direction can be predicted from the star astrometric data and the telescope geolocation data with an error negligible in comparison to that of image positioning. The FoV clocking error translates into object positioning error as $dr \tan(da)$, where dr is a distance between the object and reference, which typically does not exceed $10''$, da is the FoV clocking error. In particular, to get the 10 mas contribution to the object position error the clocking error should be equal to $3.5'$, which is difficult to achieve in practice. As it will be shown below, the image position and thus the reference star pass direction can be estimated with reasonable accuracy as a part of the positioning process.

The goal of the next sections will be to estimate the achievable positioning accuracy within the limits outlined above for a properly balanced imaging system design.

2.1. From mechanical to astrometric reference

The preliminary release (with stars coordinates but without proper motions and parallaxes) of the GAIA star catalog [17,18] made in mid-2016 has at least 90% sky coverage, the final release is expected at 2022 [19]. Parameters of the catalog are briefly discussed in Ref. [20]. The key feature of the GAIA catalog is its unprecedented accuracy: the star positions are measured with the errors typically not exceeding tens of

micro-arcseconds. This provides the astrometric reference with accuracy orders of magnitude better than the typical mechanical accuracy of the telescope mounts, which is rarely better than 1". Thus, the reference error, which is the main contributor in the conventional space object optical positioning techniques, is virtually eliminated.

A problem of sufficient observable reference star density related to the use of astrometric references should be addressed in detail. However, in order to estimate the reference star density it is not even necessary to have the GAIA catalog at disposal. Such information can be extracted from the standard USNO-b1 star catalog [21], which is on par with GAIA with respect to completeness (not accuracy). It is of interest to us to estimate density of the part of the star field observed from the observatory location, which "lies behind" the Geosynchronous Region that officially [22] extends within ±15° equatorial declinations and ±200 km around the Geostationary Orbit radius.

Given below are simple formulas to estimate equatorial coordinates of a GEO satellite as they are seen from the observatory ("view direction coordinates"). The view direction equatorial coordinates can then be used directly in the catalog queries for the reference stars. Also of interest are the corresponding topocentric horizontal coordinates, in particular, the telescope zenith and azimuth angles. Tables 1 and 2 show, respectively, the input and output values used in our calculations.

Elementary geometry gives for the view direction coordinates:

$$\overline{DE} = \arctan \frac{VO_z}{|VO|}, \tag{1}$$

$$\overline{HA} - HA = \frac{RE \sin HA \cos LA}{(RE \cos LA)^2 + RG^2 - (2RE RG \cos HA \cos LA)^{1/2}},$$

horizontal coordinates:

$$ZE = \arccos \frac{LZ^T VO}{|VO|}, \tag{2}$$

$$AZ = \arctan \frac{(LN \times LZ)^T VO}{LN^T VO},$$

where

$$VO = RG [\sin HA, \cos HA, \tan DE]^T - RE [0, \cos LA, \sin LA]^T$$

is a view direction vector connecting the telescope and the space object,

$$LZ = [0, \cos LA, \sin LA]^T,$$

$$LN = [0, -\sin LA, \cos LA]^T,$$

are the local zenith and local North vectors. The minimal zenith angle (for HA = 0) to observe a GEO satellite from the MSO is 41.1°, the maximal zenith angle is limited by the telescope design to 70°. This range of zenith angles is quite unfortunate because implies non-optimal AO system operation. The MKO location is closer to equator and is thus more suitable for GEO observations: the minimal zenith angle in this case is just 23.2°.

Table 1
Parameters used compute satellite view direction coordinates at the observatory location.

Notation	Value	Description
RE	6.378 × 10 ³	Earth radius, [km]
RG	35.786 × 10 ³ + RE	Geostationary orbit radius, [km]
LA	-35.3163/19.82561	MSO/MKO latitudes, [deg]
LO	149.00986/155.47322	MSO/MKO longitudes, [deg]
HA	±180°	true hour angle from observatory longitude, [deg]
DE	±15°	true geo-band declination, [deg]

Table 2
Satellite view direction output data.

Notation	Description
\overline{HA}	View direction hour angle, [deg]
\overline{DE}	View Direction Declination, [deg]
AZ	Azimuth angle of the telescope, [deg]
ZE	Zenith angle of the telescope, [deg]

Fig. 1 shows dependence of the view direction coordinates on the satellite/observatory hour angle for the MSO case.

For the sky sector observable within the geo-band it is possible to query the USNO-b1 to map the density of stars within given brightness. In particular, Fig. 2 presents star density histograms for the entire geo-band sector, its mid-line and the curve corresponding to the GEO equator as observed from MSO. In particular, 5515 stars brighter than 16th magnitude in I-band that are at most 10" away from the GEO equator trajectory can be revealed, which confirms feasibility of the astrometric reference approach.

2.2. Atmospheric turbulence

The turbulence profiles typical for the MSO and MKO locations are presented in Tables 3 and 4.

It is obvious from the tables that the MSO and MKO turbulence profiles represent nearly the two extremes: quite severe turbulence at MSO and the exceptionally calm atmosphere at the world's best observatory site in the case of MKO. Due to the favorable location and also its larger size the UKIRT telescope is able to provide, as we will show below, about the same image quality without AO as the EOS telescope with AO.

Fig. 3 gives an illustration of the anisokinetic error, an uncompensable error contributor independent of the presence of AO correction, found via Monte-Carlo simulation. The graph suggests that the lower limit for the positioning error at the edge of 10" FoV is 80 and 15 mas/frame for MSO and MKO profiles, respectively.

3. Adaptive optics

Adaptive Optics potentially can greatly improve debris positioning accuracy. Design of an AO system for the orbital tracking has certain differences from the one for astronomical purposes. In particular, natural guide stars cannot be used as light beacons for the wavefront sensing because of their insufficient flux: the limiting NGS magnitude providing decent AO performance is around V9 (V-band is used to separate AO and imaging channels), which is an extremely rare occasion. This necessitates the use of the Laser Guide Star (LGS) and, as it is seen from Fig. 4, for a typical expected photon return from the Na LGS it is possible to achieve ~ 16% Strehl Ratio in I-band, at 50° zenith angle and with optimized AO system parameters, which can be considered a good result for such strong turbulence as it is expected at MSO. The differential position measurement insensitive to TT greatly simplifies the AO system design. Desire to keep the system simple also necessitates a single-conjugate (single Wavefront Sensor (WFS) and single Deformable Mirror (DM) and single LGS) design (see Table 5).

Performance of such a system is good only for small neighborhood of the guide star limited by the anisoplanatic angle θ_0 . For the turbulence profile typical for the MSO location (see Table 3) its value is around 1.2" in I-band (observation band), which, according to the AO performance simulations, guarantees at least 10% Strehl Ratio at only 3" offset (Fig. 4) and effectively sets the size of the imaging system Field of View (FoV).

Fig. 5 presents the camera image comparison for the cases of AO turned off and on, which clearly illustrates the usefulness of AO system, even the one capable of achieving only 16% Strehl. In particular, the average short-exposure (TT-excluded) full width at half maximum (FWHM) at FoV center of the uncorrected star image for the EOS imaging channel is around ~ 500 mas whereas the AO-corrected FWHM reduces

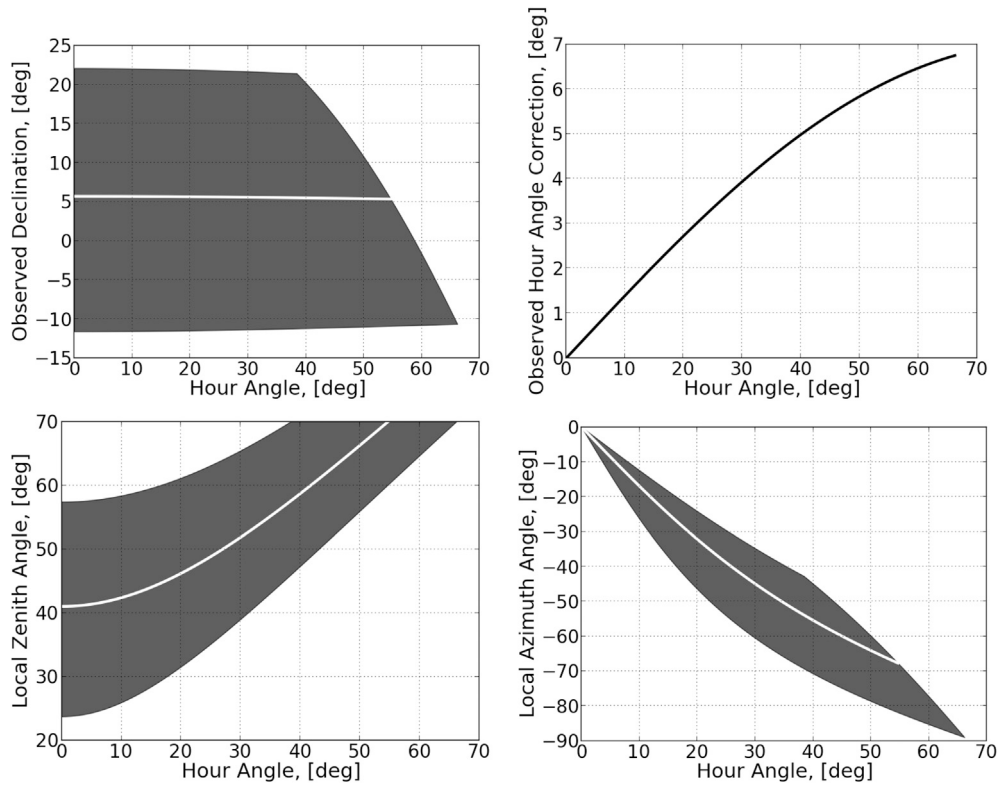


Fig. 1. GEO satellite view direction and horizontal coordinates variations as a function of declination and hour angle. The area borders correspond to the $\pm 15^\circ$ geo-band borders and the 70° zenith angle limitation. Central line corresponds to equator. Note that the part of GEO observable from MSO is about $\pm 55^\circ$.

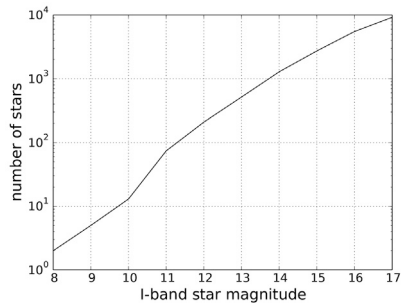
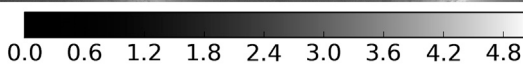
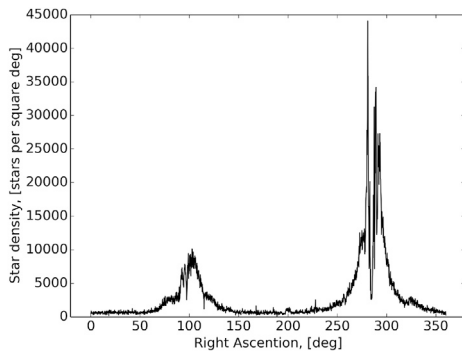


Fig. 2. Center: histogram of stars brighter than I-band 16th magnitude within geo-band observable from MSO. Up: The cross-section of the same histogram along the sector center. Down: number of stars that are closer than $10''$ to the GEO equator trajectory and brighter than a given I-band magnitude, summed over 360° .

Table 3

4-layer atmospheric turbulence model for the Mount Stromlo Observatory location.

Layer altitudes	(9000.,6000.,400.,0.) m
Layer relative weights	(0.1,0.2,0.2,0.5)
Layer wind velocities	(25.,20.,15.,10.) m/s
Layer wind directions	collinear, along x-axis (worst case)
Turbulence statistics	Von Karman
Fried parameter r_0 at $0.5 \mu\text{m}$	5 cm
Outer scale L_0	20 m
Anisoplanatic angle at 50° zenith	$1.2''$ in I-band
Greenwood frequency at 50° zenith	97.2 Hz in I-band

Table 4

6-layer atmospheric turbulence model [23] for the Mauna Kea Observatory location.

Layer altitudes	(12600.,10400.,8000.,5500.,2850.,0.) m
Layer relative weights	(0.06,0.05,0.05,0.07,0.25,0.52)
Layer wind x-velocities	(-11.0,-1.0,1.8,0.,1.8,-1.0) m/s
y-velocities	(-2.5,15.0,2.0,-11.,-16.5,-17.0) m/s
Turbulence statistics	Von Karman
Fried parameter r_0 at $0.5 \mu\text{m}$	17.9 cm
Outer scale L_0	20 m
Anisoplanatic angle at 30° zenith	$4.4''$ in I-band
Greenwood frequency at 30° zenith	23.5 Hz in I-band

to ~ 150 mas. Notably, the uncorrected FWHM in UKIRT case is also around 150 mas.

4. Positioning algorithm

Positioning is the process of extraction the object position information from a sequence of images obtained during the simultaneous observation of a reference star and a space object. The assumed observation scenario that requires a positioning stage is the following:

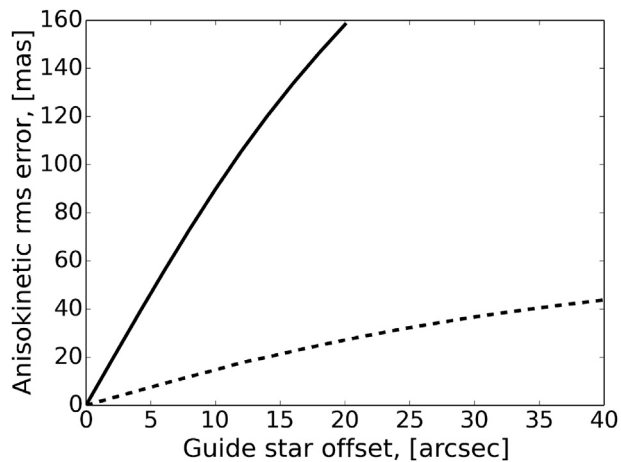


Fig. 3. The anisokinetic error as a function of FoV obtained from Monte-Carlo simulation on 100 random realizations of the Mount Stromlo at 50° zenith angle (solid line) and Mauna Kea at 30° zenith angle (dashed line) turbulence profiles.

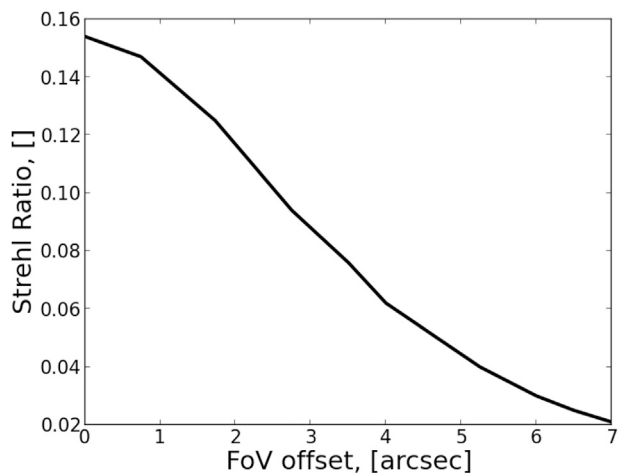


Fig. 4. Strehl ratio dependence on field of view. Frame rate 2000 Hz, LGS flux corresponds to 2000 photons/s/m² at zenith. Result of AO system Monte-Carlo simulation on 100 random realizations of the Mount Stromlo turbulence profile, observation in I-band, 50° zenith angle.

Table 5
The EOS telescope AO system parameters.

Telescope	1.8-meter EOS SLR telescope
Atmospheric turbulence model	“Mount Stromlo” profile, Table 3
Beacon	Na LGS, 1.5 m off-axis launch, centered on-axis
Beacon flux	2000 photon/cm ² /s at zero zenith angle,
Zenith angle	50°
WFS type	Shack-Hartmann, 16×16 square lenslets
WFS camera	OCAM2k [24] 240 × 240 EMCCD
pixel size on sky	1.33”
WFS camera read noise	0.5 e ⁻ /pixel
WFS channel QE/throughput	0.45/0.35
WFS camera frame rate	2000 Hz (optimal)
DM model	ALPAO 277 [25], realistic lab-measured influence functions
DM conjugation	pupil
AO reconstructor	Least Squares with SVD cutoff 10% (optimal)
WFS/reconstructor lag	2 frames
Integrator	first order, gain 0.3, leak 0.05 (optimal)
Tip-tilt correction	turned off
Optimized Strehl ratio	16% in I-band and at FoV center

- Based on an a priori data from the time measurements, space object and star catalogs an approximate position and a time slot are

calculated during which the space object can be observed simultaneously with a reference star bright enough to perform position measurements.

- The telescope is directed to the space object: since the object is being on the GEO it is quasi-stationary with respect to the observer and thus it is wise to keep it stationary at the FoV because the telescope mount will not move. Then the reference star will move with respect to the object at the Earth rotation speed 15”/second. The true velocity of the reference star with respect to the object is subject to measurement. Since it is not accurately known in advance where the reference star will pass with respect to the object, it is optimal to keep the object in the FoV center.
- During the pass of the reference it is possible to make a series of accurately timed exposures formed either by a mechanical chopper or by the electronic frame transfer in the camera serving for the same purpose. The intent of multiple exposures is: 1) to reduce the motion blur due to tip-and-tilt errors, 2) to be able to connect the object position in the image with the time of passage and, therefore, to measure not only position but also motion phase and velocity.
- The object trajectory is extractable from a series of timed image frames obtained at each simultaneous reference star and object observation (the “rendezvous”) by watching the four transit parameters with straightforward interpretation:
 1. the transit direction α in the telescope FoV (crucial for subsequent correction for the FoV rotation with respect to a stationary coordinate system);
 2. the transit pass-point position x_0 defined as a point of the reference star trajectory closest to the space object;
 3. the transit zero-point z_0 corresponding to an arbitrary fixed time origin;
 4. the transit velocity v .
- That is what we will call positioning.
- Repetition of the procedure for the multiple rendezvous involved multiple references allows to bootstrap the information about the space object.

The positioning process is a set of image processing algorithms applied to the images in the following order:

1. De-noising is applied to each image in the sequence in order to increase its signal-to-noise ratio. Since the image photon noise is statistically orthogonal to the readout and background noise, the latter noises are efficiently suppressed by the background subtraction and local averaging using Gaussian filter as it is illustrated on Fig. 6.
2. Find-and-identify algorithm is applied to discover a reference/object pair in each image. Since the sought reference star and space object images look in most cases as well-isolated bell-shape maxima and it is unlikely to see more than two bright objects within the 20” field of view, the reasonably efficient find-and-identify algorithm consists of exhaustive search of two brightest pixels among the all image local maxima. Obviously, if the reference and object spots overlap, the algorithm will fail, but this will create an outlier, which is quite efficiently detected and ignored on the integration stage. Another problem associated with the so primitive spot identifier is its inability to tell the object from the reference. This is solved on the pre-integration stage when spot positions from all frames are identified: since the reference transit direction is approximately known a priori, the spot positions can be ordered to lie along the reference transit vector, which may also fail in the case of the spot overlap creating maybe another outlier.
3. Positioning algorithm is applied to find the object coordinates with respect to the reference: for the ordered pairs of reference and object maxima this stage can coarsely be reduced to subtraction of the maxima coordinates but, in order to achieve sub-pixel accuracy, the neighborhoods of the maxima are up-sampled using a simple Fourier domain zero padding algorithm [26].

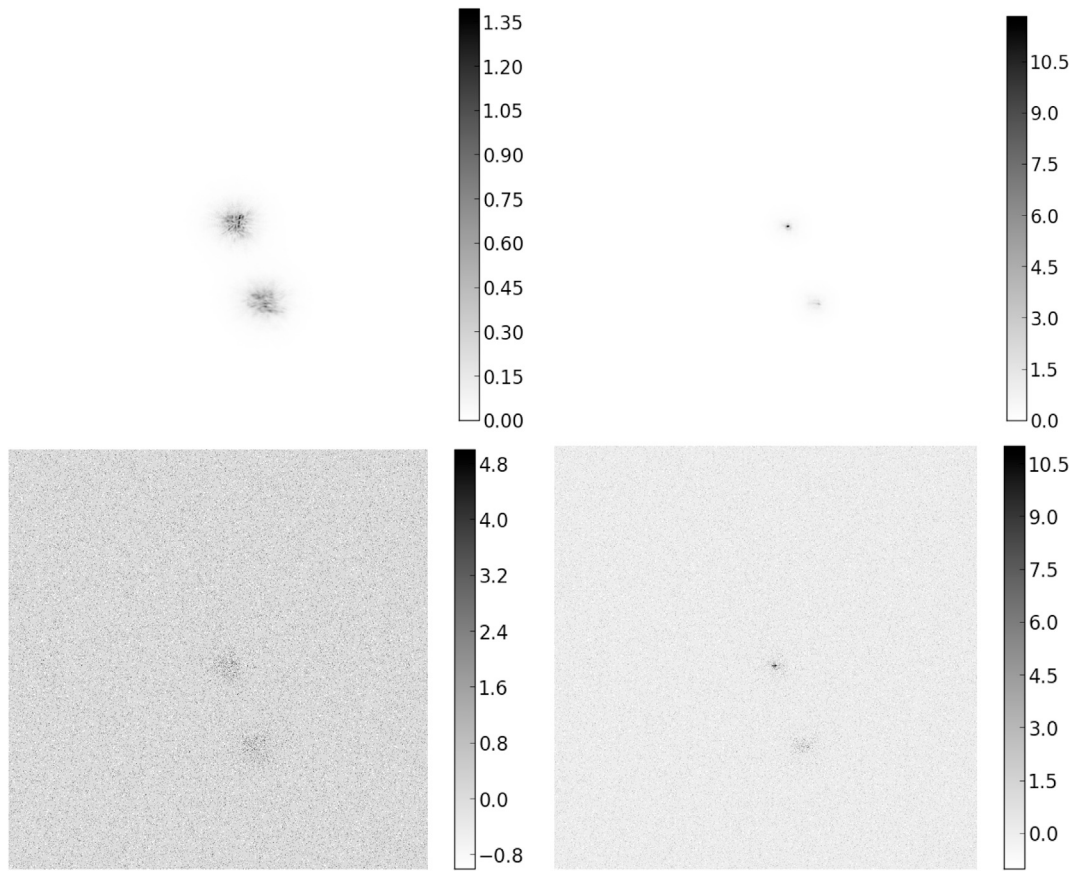


Fig. 5. A pair of GEO object (in the center) and reference star (passes horizontally at 4'' offset from the FoV center) imaged without (left) and with AO (right). Upper row shows optical flux distribution on the camera in units of [photons/exposure/pixel]. Lower row shows noisy images in units of [photo-events/exposure/pixel]. It is seen that AO improves pixel intensities by almost an order of magnitude.

4. Integration algorithm is applied to the whole image sequence in order to estimate the transit parameters from all the images together as if they were one long exposure. It is assumed that, within the quite small telescope FoV, the debris trajectory can be considered a straight line $ax + b$, where the a, b -parameters are conveniently found by linear regression [27] from the sequence $[x_k, y_k]_{k=1}^N$ of the difference vector pairs found for each image frame. Since both position and pass-time need to be estimated from the recorded frames it is convenient to replace the line equation with its parametric analog

$$x(t) = a_x t + b_x,$$

$$y(t) = a_y t + b_y,$$

describing both position and velocity from two sequences of "time-tagged" coordinates $[x(t_k), y(t_k)]_{k=1}^N$. Regression $(a_x, a_y; b_x, b_y)$ -parameters are found from the position estimates $[x(t_k), y(t_k)]_{k=1}^N$ as:

$$\begin{bmatrix} a_x & a_y \\ b_x & b_y \end{bmatrix} = \begin{bmatrix} T^T T & T^T I \\ T^T I & I^T I \end{bmatrix}^{-1} \begin{bmatrix} X^T T & Y^T T \\ X^T I & Y^T I \end{bmatrix},$$

where $X = \{x(t_k), k = 1, N\}$, $Y = \{y(t_k), k = 1, N\}$, $T = \{t_k, k = 1, N\}$, $I = \{1, k = 1, N\}$. The transit parameters can be easily found from the regression coefficients:

- (a) transit direction: $a = a_y/a_x$;
- (b) transit point:

$$x_0 = \frac{1}{a^2 + 1} [-ab, b], \quad b = b_y - ab_x;$$

- (c) transit zero-point: $z_0 = [b_x, b_y]$;
- (d) transit velocity: $v = [a_x, a_y]$.

An efficient outlier detection algorithm can be built iteratively by applying the regression to a data set, finding a distance from each point to the regression line, excluding too remote points and re-applying the regression to the reduced data set. The median distance proves to be much more reliable outlier detection criterion than the mean squares.

In the summary, the positioning algorithm takes a set of images and the additional parameters: width of median filter for background estimation, width of Gaussian local averaging filter for de-noising, reference motion direction estimate, and the median distance fraction for the outlier criterion. Fig. 6 illustrates all stages of the positioning process.

5. End-to-end simulations

Accuracy of GEO spacial object positioning was estimated by means of end-to-end Monte-Carlo simulations that bind together the computer models for turbulence propagation, image formation, AO system operation and image processing for space object positioning. We restricted ourselves to the two realistic imaging system configurations: the EOS telescope equipped with the prospective LGS AO system configuration (see Table 5) and 2) the UKIRT telescope imaging system without AO. Parameters of both imaging channels are presented in Table 6.

The imaging system parameters were also tuned for each individual combination of the reference offset and brightness. In particular, the optimal positioning accuracy in the uncorrected case was achieved for the imaging camera pixel size roughly doubled with respect to the Nyquist sampling, the optimal imaging frame rate ranges from 20 to

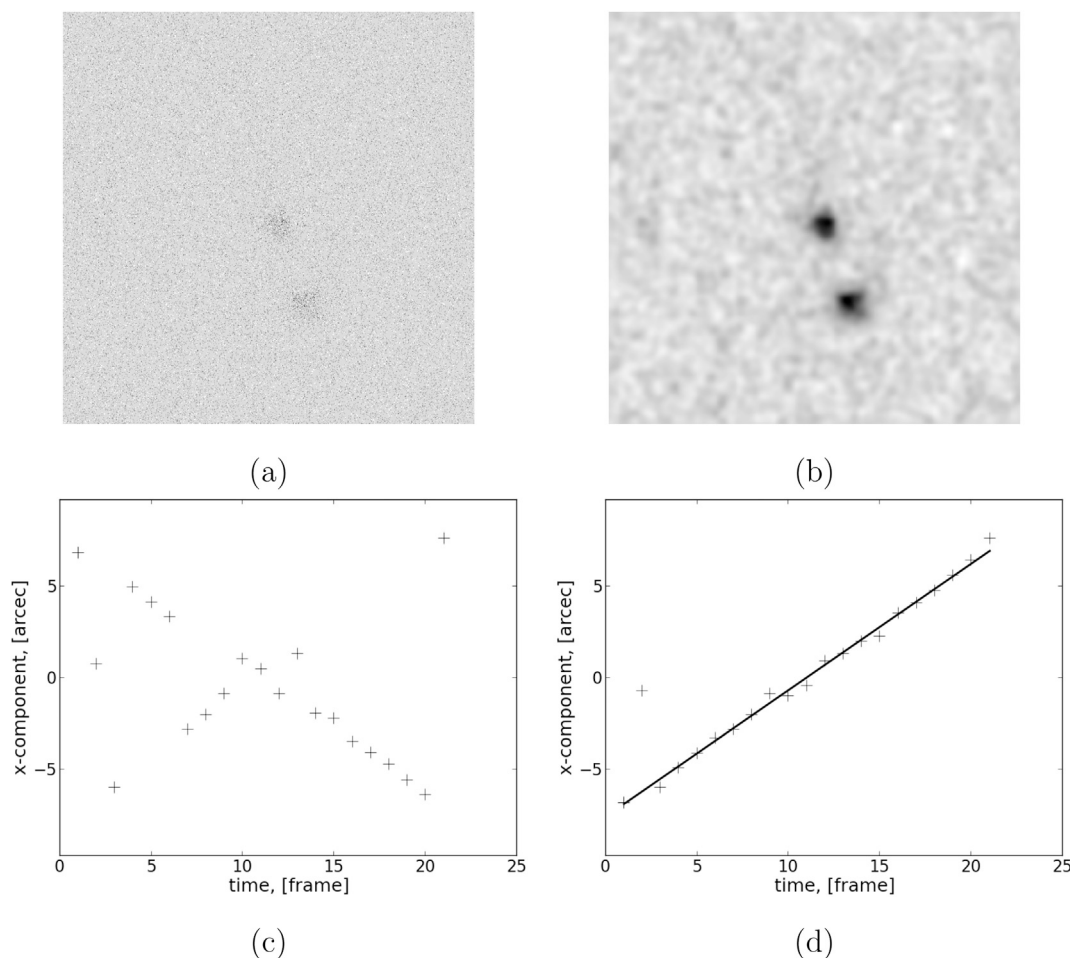


Fig. 6. Illustration of the positioning image processing sequence. (a) Initial noisy image corresponding to object and reference source of 14th magnitude at 20 Hz frame rate. EOS system, AO correction is turned off. (b) Read noise and background suppression using standard astronomical image processing algorithms [28,29]: first, image background level is estimated via median filter with 3×3 kernel and subtracted, then the zero-mean noise is suppressed by the Gaussian filter with $\sigma = 10$ pixels. (c) difference vectors after find-and-identify, with sign flips and outliers. (d) difference vectors after point ordering and iterative regression with outlier detection.

40 Hz, the optimal Gauss filter full width at half maximum (FWHM) is roughly equal to that of the image spot, the best outlier cutoff is equal to twice median variation from the regression line. The Monte-Carlo simulation parameters are described in Table 7.

Figs. 7 and 8 present graphically the results of simulations for the case when the imaging camera noise is turned off while the atmospheric turbulence is still present. This allows to see the impact of turbulence alone and, in particular, the anisokinetic error. Figs. 9 and 10 present the results of simulations with camera noise included. These graphs give an estimate of the expected full positioning error with all major contributors included. As it can be concluded from comparison of noiseless and noisy

results, the main contributor to the positioning error is the atmospheric anisokineticism.

Note that the graphs (a) on the figures mentioned above, i.e. the main, positioning errors, do not include the clocking contribution. This contribution can be estimated from graphs (d) (if no external means for image clocking estimation are used) using the formula from Section 2, which, obviously, can double the error in the case of large offsets. Looking for the ways to reduce this contribution may be a direction of the future research.

6. Conclusions

A method for high accuracy, Adaptive Optics aided optical

Table 6
Parameters of the EOS and UKIRT telescope imaging channels.

Parameter	EOS	UKIRT
Observation zenith angles, [°]	41–70	23–60
Imaging camera model	Hnu512 [12]	pco.edge 4.2 [13]
Imaging camera type	EMCCD	sCMOS
Imaging camera read noise, [$e^-/pixel$]	0.3	0.8
Imaging camera sampling, [mas on sky]	100	100
Imaging camera Field of View, [$''$ on sky]	51.2	204.8
Imaging camera maximal frame rate, [Hz]	63	40
Imaging channel bandwidth	$R + I$	$R + I$
Imaging channel QE/throughput	0.875/0.35	0.875/0.35
Imaging pass time, [s]	1	1
Reference star angular velocity, [$''/s$]	15	15
Debris/reference magnitude limit, [m_{I+R}]	15	19
Sky background [$m_{I+R}/arcsec^2$]	18	19

Table 7
Parameters of the Monte-Carlo simulations for the GEO object positioning accuracy.

Telescope	EOS	UKIRT
Reference offset range	0''–8''	0''–40''
Observation zenith angle	50°	30°
Source magnitude range	$m_{I+R} = 16..12$	$m_{I+R} = 19..14$
AO system	as described in Table 5	no AO
Imaging systems	as described in Table 6	
Space object	a point source on GEO at FoV center	
Reference star	a point source at infinity traveling horizontally in FoV at 15''/s	
Positioning algorithm	as described in Section 4 with parameters optimized manually for each case	
Number of Monte-Carlo runs	100	

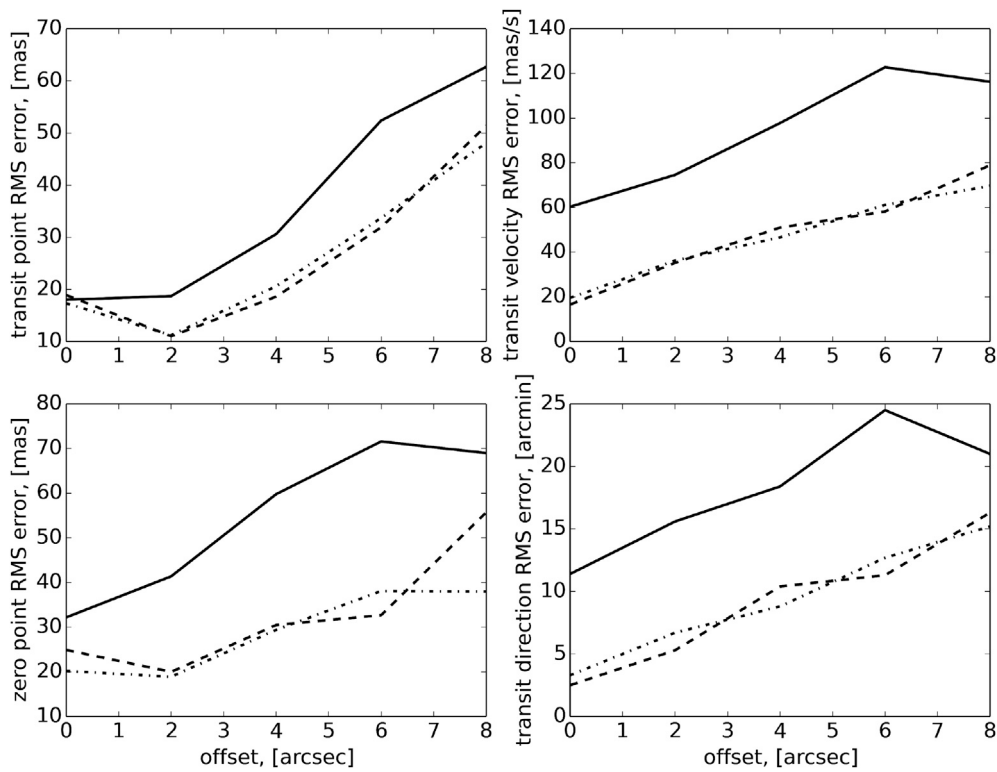


Fig. 7. RMS errors in the transit parameters estimated from the Monte-Carlo simulations with parameters described in Table 7 as a function of reference star offset. Noiseless case as an illustration of purely turbulence-induced errors. EOS system. Solid lines correspond to no AO correction, dashed lines correspond to noisy AO correction, dash-dot lines correspond to noiseless (best possible) AO correction.

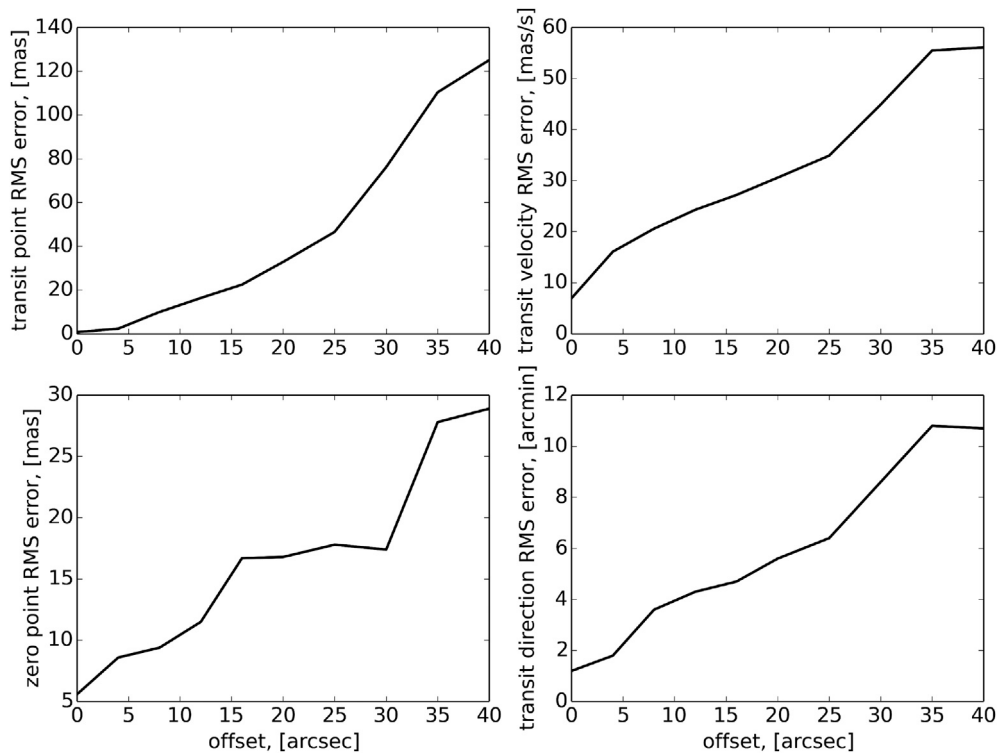


Fig. 8. RMS errors in the transit parameters estimated from the Monte-Carlo simulations with parameters described in Table 7 as a function of reference star offset. Noiseless case as an illustration of purely turbulence-induced errors. UKIRT system. Solid lines correspond to no AO correction.

positioning of the Geostationary Orbit (GEO) space debris based on detection of astrometrically accurate reference star transits in the debris

close vicinity is proposed and analyzed in this paper. The star catalog analysis reveals quite ample number of potential reference stars in the

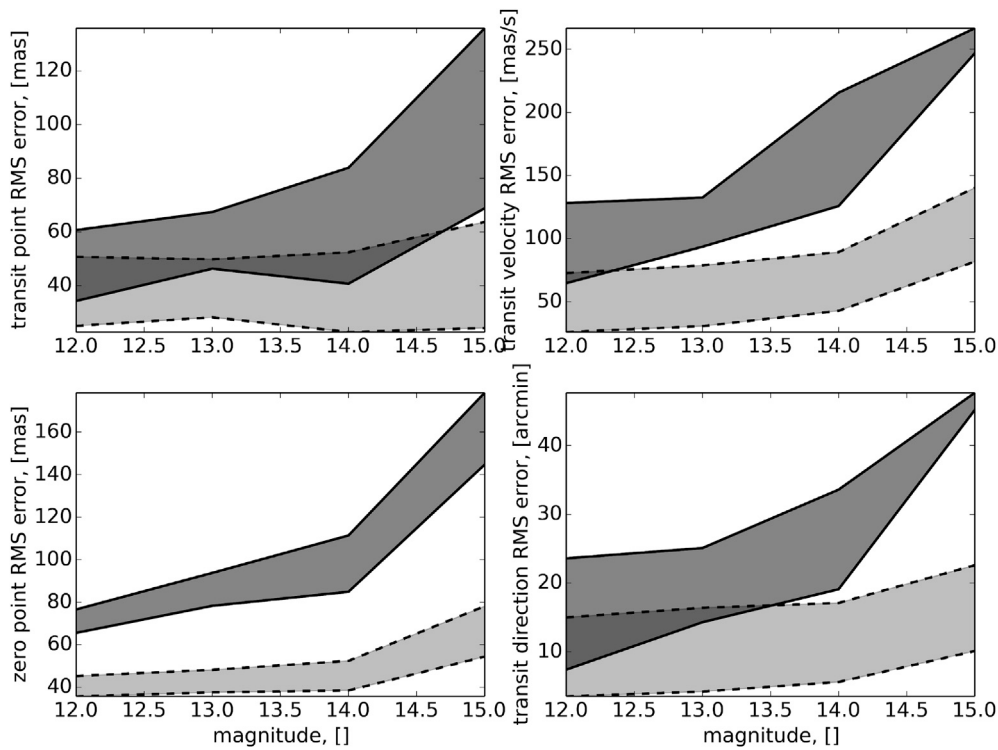


Fig. 9. RMS errors in the transit parameters estimated from the Monte-Carlo simulations with parameters described in Table 7 as a function of source brightness. EOS system. Both turbulence and noise included. Solid lines delimit the area between 0'' and 8'' offsets for no AO correction, dashed lines are the same for noisy AO-corrected case.

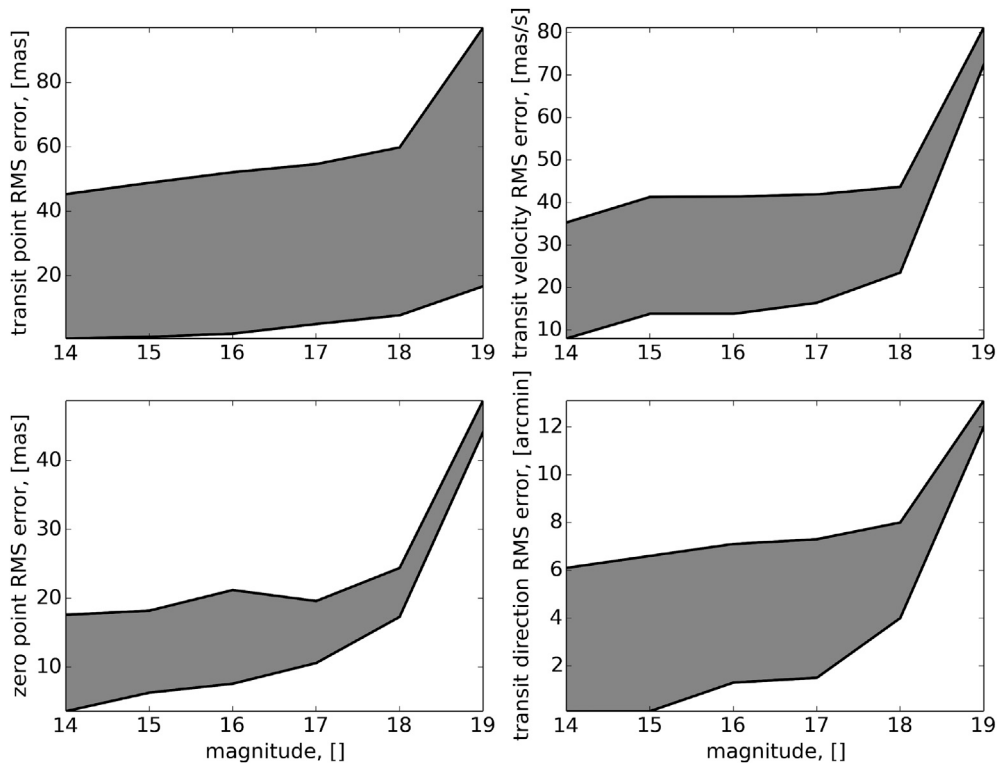


Fig. 10. RMS errors in the transit parameters estimated from the Monte-Carlo simulations with parameters described in Table 7 as a function of source brightness. UKIRT system. Both turbulence and noise included. Solid lines delimit the area between 0'' and 25'' offsets for no AO correction.

vicinity of the GEO making the proposed method feasible. Accuracy of the space debris positioning is estimated through the thorough end-to-end simulations that include models for the debris motion, AO system operation and noisy pixelated image formation. It has been shown that an

imaging system design consisting of:

- the existing 1.8-meter telescope at the Mount Stromlo Observatory location equipped with an AO system,

- an off-the-shelf low-noise EMCCD camera-based imaging channel with 30% overall quantum efficiency,
- a single Laser Guide Star (LGS) with return flux on the ground equal to 2000 photons/m²/s;
- Single-Conjugate LGS-based Adaptive Optics channel with overall 20% quantum efficiency using an off-the-shelf low-noise fast CMOS camera for the wavefront sensing or
- the existing 3.8-meter telescope, not equipped with AO but enjoying extremely calm atmospheric conditions of the Mauna Kea location and
- an off-the-shelf low-noise sCMOS camera-based imaging channel with 30% overall quantum efficiency

are both capable of achieving ~ 40 mas positioning accuracy (direction error excluded) for the debris brightness corresponding up to 15th (19th) magnitude in strong $r_0 = 5$ cm turbulence and at large zenith angles thanks to AO (in case of MSO) and calm atmosphere (in the MKO case). Also proposed is an efficient combination of image processing algorithms with minimal number of user-supplied parameters with potential for full automation of the debris tracking procedures. The following practical findings are worth mentioning:

- Linear image denoising via the local averaging in combination with iterative linear regression for outlier detection results in a very reliable image processing algorithm for space object positioning, which does not require further user interventions.
- While positioning accuracy of the image processing algorithms as such is very high it is overwhelmed with the contribution of quite strong turbulence typical to Mount Stromlo Observatory site and further complicated by operation at large zenith angles. The AO system, however, copes with those complications quite efficiently.
- Better observatory location both with respect to proximity to the equator and turbulence conditions brings up the full strength of the proposed differential positioning approach.
- Clocking error contribution is significant and a method for its reduction is desirable.

The presented results make the basis for practical implementation of the proposed debris tracking system in the future. Important milestones on this way will include integration of the sparse debris positioning data obtainable with the described technique into the complete orbit determination algorithm and building of the actual imaging/AO module.

Acknowledgements

This work has made use of data from the European Space Agency (ESA) mission *Gaia* (<https://www.cosmos.esa.int/gaia>), processed by the *Gaia* Data Processing and Analysis Consortium (DPAC, <https://www.cosmos.esa.int/web/gaia/dpac/consortium>). Funding for the DPAC has been provided by national institutions, in particular the institutions participating in the *Gaia* Multilateral Agreement.

The authors would like to acknowledge the support of the Cooperative Research Centre for Space Environment Management (SERC

Limited) through the Australian Governments Cooperative Research Centre Programme.

References

- [1] D.S. McKnight, Frank R. Di Pentino, New insights on the orbital debris collision hazard at GEO, *Acta Astronaut.* 85 (2013) 73–82.
- [2] I. Molotov et al., ISON worldwide scientific optical network, in Proceedings of the Fifth European Conference on Space Debris, Proceedings of the Conference Held 30 March - 2 April, 2009 in Darmstadt, Germany. Edited by H. Lacoste. ESA-SP Vol. vol. 672.
- [3] T. Flohrer, T. Schildknecht, R. Musci, Proposed strategies for optical observations in a future European Space Surveillance network, *Adv. Space Res.* 41 (2008) 1010–1021.
- [4] T. Flohrer, T. Schildknecht, R. Musci, E. Stoeken, Performance estimation for GEO space surveillance, *Adv. Space Res.* 35 (2005) 1226–1235.
- [5] R. Scott, B. Bennett, Canadian surveillance of space concept demonstrator – metric accuracy and limiting magnitude assessment, *Acta Astronaut.* 57 (2005) 302–311.
- [6] A. Tokovinin, Adaptive Optics Tutorial, <http://www.ctio.noao.edu/~atokovin/tutorial/intro.html>.
- [7] R. Scott, A. Ellery, An approach to ground based space surveillance of geostationary on-orbit servicing operations, *Acta Astronaut.* 112 (2015) 56–68.
- [8] R. Scott, A. Ellery, Speckle Interferometry tracking of on-orbit servicing in geostationary orbit, *J. Spacecr. Rockets* 53 (2016) 433–447.
- [9] GAIA mission. <http://sci.esa.int/gaia/>.
- [10] The United Kingdom Infra-Red Telescope, www.ukirt.hawaii.edu.
- [11] Electron Multiplying Charge Coupled Device. https://de.wikipedia.org/wiki/Electron_multiplying_charge_coupled_device.
- [12] The NuVu Hnu 512 EMCCD camera, <http://www.nuvucameras.com/products/hnu-camera/>.
- [13] The PCO Edge 4.2 camera, <https://www.pco-tech.com/scmos-cameras/pcoedge-42/>.
- [14] M. Bourez-Laas, A. Klotz, G. Blanchet, M. Boer, E. Ducrotte, Algorithms improvement in image processing for optical observations of artificial objects in geostationary orbit with the TAROT telescopes, *Proc. SPIE 7000 Opt. Digital Image Process.* 700020 (2008).
- [15] M.A. van Dam, R.J. Sasiela, A.H. Bouchez, et al., Angular anisoplanatism in laser guide star adaptive optics, *Proc. SPIE 6272* (2006) 627231.
- [16] Laser Guide Star Tutorial, <http://www.ctio.noao.edu/~atokovin/tutorial/part4/lgs.html>.
- [17] Gaia Collaboration, T. Prusti, J.H.J. de Bruijne, A.G.A. Brown, A. Vallenari, C. Babusiaux, C.A.L. Bailer-Jones, U. Bastian, M. Biermann, D.W. Evans, et al., *The Gaia mission*, *A&A* 595 (2016b) A1.
- [18] First release of GAIA star catalog http://1016243957.rsc.cdn77.org/Gaia/gaia_source/.
- [19] GAIA mission data release strategy. <http://www.cosmos.esa.int/web/gaia/release>.
- [20] M. A. Murison, H. C. Harris, Taking advantage of (anticipated) gaia astrometry ... and what about the bright stars? Conference: American Astronomical Society Division on Dynamical Astronomy. Philadelphia, PA, USA, Volume: vol. 45.
- [21] The USNO-B1.0 Catalog, <http://tdc-www.harvard.edu/catalogs/ub1.html>.
- [22] IADC Space Debris Mitigation Guidelines, Inter-agency space debris coordination committee, 2007. ADC-02-01, <http://www.iadc-online.org/Documents/IADC-2002-01,%20IADC%20Space%20Debris%20Guidelines,%20Revision%201.pdf>.
- [23] P. Massioni, L. Gilles, B. Ellerbroek, Adaptive distributed Kalman filtering with wind estimation for astronomical adaptive optics, *JOSA A* 32 (2015) 2353–2364.
- [24] The FirstLight OCAM2k EMCCD camera, <http://axiomoptics.com/llc/ocam%20B2k/>.
- [25] <http://www.alpao.com/adaptive-optics/20-services/110-adaptive-optics-deformable-mirrors.html>.
- [26] Image upsampling in frequency domain, <http://angeljohnsy.blogspot.com/2015/11/upsampling-in-frequency-domain.html>.
- [27] Simple Linear Regression, http://en.wikipedia.org/wiki/Simple_linear_regression.
- [28] R.C. Stone, A comparison of digital centering algorithms, *Astron. J.* 97 (1989) 1227–1237.
- [29] K.J. Mighell, Algorithms for CCD stellar photometry, astronomical data analysis software and systems VIII, *ASP Conf. Ser.* 172 (1999).